Noble-metal nanoparticles and short pulses for nanomanipulations: theoretical analysis

Gili Bisker* and Dvir Yelin

Department of Biomedical Engineering, Technion—Israel Institute of Technology, Haifa 32000, Israel
*Corresponding author: bisker@tx.technion.ac.il

The rapid temperature change and the near-field enhancement resulting from resonant interactions between short laser pulses and noble-metal nanoparticles could be utilized for precise manipulations of matter on a nanometric scale. Here, we present a theoretical study of the relative effects of various experimental parameters, including pulse duration, irradiance, and wavelength, and a particle's substance, size, and shape. We show that spatially confined, local nanometric interactions between a particle and its near surroundings are feasible using 50 nm gold and silver nanospheres illuminated by laser pulses shorter than 70 fs and 90 fs, respectively, with no particle melting and minimal collateral damage. The results of this work could be useful for researchers in various fields, who aim at manipulating matter on the smallest possible scales, with high specificity and accuracy.   © 2012 Optical Society of America

OCIS codes: 140.3440, 140.7090, 190.4180, 260.5210, 290.5850.

1. INTRODUCTION

The ability to precisely manipulate biological targets on a sub-micrometer scale is important for many emerging fields in biotechnology and nanotechnology. Continuous-wave and short pulse lasers have been used for numerous clinical applications that require localized interventions [1–3], although their effects often extend beyond the diffraction limit due to heat diffusion and/or excessive mechanical stress. In recent years, femtosecond pulse lasers have been shown useful for targeting cellular and subcellular structures [4–6], including ablation of cytoskeleton filaments and mitochondria [7], dissection of human chromosomes [8], membrane perforation for DNA transfection [9], and cutting individual axons [10]. While optical microscopy has already crossed the diffraction barrier [11,12], the manipulations of matter on the scale of less than a few tens of nanometers, 1 order of magnitude below the diffraction limit, still remain a challenge using optics alone.

Because of their high absorption of light at resonant wavelengths, noble-metal nanoparticles [13–15] have been shown capable of bridging the gap between the microscale and the and nanoscale, allowing specific nanosurgery and nanomanipulation [16]. A wide range of functionalized noble-metal nanoparticles have been demonstrated useful for biomedical applications such as microscopy [17–20], drug delivery [21,22], and therapy [23,24]. When resonantly illuminated with intense short laser pulses, gold and silver nanoparticles affect their nearby environment through a combination of three main processes: (1) light absorption by the particle causes heat accumulation, which gradually diffuses to its environment after a few picoseconds [25]; (2) if sufficient energy is rapidly accumulated within the particle, an acoustic shock wave is formed as a result of thermal expansion and vaporization [26]; (3) the strong fields near the particle surface [27] interact with the surrounding medium and, at sufficiently high intensities, ionize it, producing low density plasma around the

particle [28]. The exact contribution of each one of these processes to the total effect strongly depends on the pulse irradiance, duration, and wavelength, as well as on the particle's shape and substance. The interaction between nanosecond pulses and nanoparticles has been shown effective for nanofabrication of azopolymer film [29], thermolysis of cancerous cells [30], and membrane permeabilization [31]. With significantly lower fluence threshold for ablation [32] and smaller thermal effects [28,32], femtosecond pulses were combined with nanoparticles for nanoprocessing of silicon surfaces [28,33], ablation of human chromosomes [34], and photo-thermal therapy of cancer [19].

A particularly attractive approach for inducing a true nanometric effect would be to utilize the strong resonant near-field enhancement for ionizing molecules close to the particle's surface. Such a process has the potential to be truly nanometric, since the volume of the field enhancement is comparable or even smaller than the nanoparticle itself. Still, accumulation of excessive heat within the nanoparticles due to the high absorption cannot be neglected in most cases, and often compromises the locality of the total effect. Moreover, high pulse fluence may cause particle melting and, as a result, loss of its optical and chemical function. Nonspherical nanoparticles such as nanorods are particularly sensitive to this effect, having a tendency to change their morphology and lose their original function [35–38].

In this work, we theoretically study the interaction between ultrashort (less than 10 ps) pulses and noble-metal nanoparticles, with emphasis on the relative roles of thermal and ionization processes, for inducing effects that are limited to the smallest possible dimensions. The main motivation of this study is to better understand the synergy between short pulses and small particles to manipulate biological targets such as cells and tissues, on a nanometric scale. Owing to the high biocompatibility of gold nanoparticles and the low toxicity
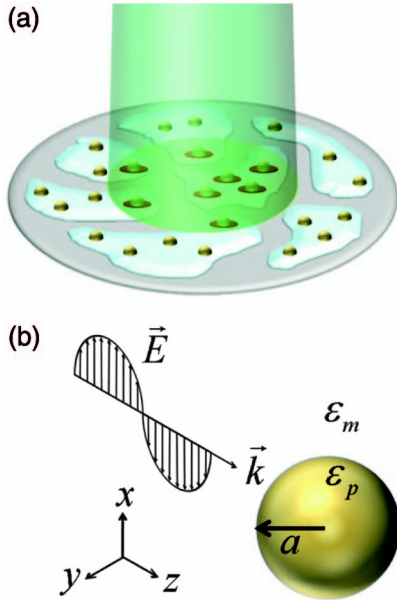
Fig. 1. (a) Schematic illustration of nanomanipulations of cells in culture using resonant pulse illumination of targeted gold nanoparticles. (b) Schematic of the interaction geometry between polarized light and a dielectric nanospheres of radius a.

of visible-infrared light, this approach for nanomanipulations of biomaterials could be attractive for a wide range of applications in the biomedical fields. An example for such application is the disruption of the plasma membranes of specifically targeted cells for allowing transport of various molecules into the cells [39] and promoting specific cell death [16] [Fig. 1(a)]. Using numerical simulations based on Mie theory and the rate equations for free electrons density [40], we outline an experimental parameter space for inducing desired nanometric photo-thermal and/or photo-ionization effects.

2. ABSORPTION AND SCATTERING BY NOBLE-METAL NANOSPHERES

Our physical model for the light-particle interaction, schematically illustrated in Fig. 1(b), includes [41] a linearly polarized plane wave with a center wavelength λ_0 propagating along the $+z$ axis, and a dielectric sphere of radius a and dielectric constant ε_p surrounded by a medium characterized by a dielectric constant ε_m. The majority of pulse bandwidths considered in this work are much narrower than the plasmonic bands of the nanoparticles, and hence could be approximated as monochromatic for determining absorption and scattering coefficients. Extremely short pulses with durations of 5–10 fs may have bandwidths that approach or even exceed those of the plasmonic resonances; these pulses may require a small correction factor to account for the narrowing of the effective interaction

bandwidth. Such a correction factor is beyond the scope of this work, and will be neglected throughout this section.

A. Dielectric Constant of Nanoparticles
The dielectric functions of metals is the sum of the dielectric constants of free electrons $\varepsilon_{\text{free}}$ and bound electrons $\varepsilon_{\text{bound}}$ [42,43]:

$$\varepsilon_p = \varepsilon_{\text{free}} + \varepsilon_{\text{bound}}, \tag{1}$$

where the bound electrons contribution is assumed to be independent of the particle's dimension [44], and the contribution of the free electrons is given by [44]

$$\varepsilon_{\text{free}} = 1 - \frac{\omega_p^2}{\omega_0^2 + i\omega_0\gamma_{\text{free}}}, \tag{2}$$

where $\omega_0 = 2\pi c/\lambda_0$ denotes the central angular frequency of the plane wave, ω_p denotes the plasma frequency, and γ_{free} denotes the damping constant. For small particles, typically a few nanometers in diameter, electron scattering by the particle surface needs to be considered, making the damping coefficient a function of the particle's radius according to [45]

$$\gamma_{\text{free}}(a) = \gamma_{\text{bulk}} + A\frac{v_F}{a}, \tag{3}$$

where γ_{bulk} denotes the damping constant of bulk material, ν_F denotes the Fermi velocity of the free electrons, and A is a dimensionless scattering constant. For calculating the optical properties of gold and silver particles, we use the physical parameters summarized in Table 1.

B. Absorption and Scattering Efficiencies
Following Mie theory [41], the extinction, scattering, and absorption efficiencies, denoted by Q_{ext}, Q_{sca}, and Q_{abs}, respectively, are defined as the ratios between the corresponding physical and the geometrical cross sections of the particle, and are given by [27]

$$Q_{\text{ext}} = \frac{2}{x^2}\sum_{l=1}^{\infty}(2l+1)\text{Re}(a_l+b_l), \tag{4}$$

$$Q_{\text{sca}} = \frac{2}{x^2}\sum_{l=1}^{\infty}(2l+1)(|a_l|^2+|b_l|^2), \tag{5}$$

and

$$Q_{\text{abs}} = Q_{\text{ext}} - Q_{\text{sca}}, \tag{6}$$

where

Table 1. Physical Constants of Gold and Silver Nanoparticles

	Parameter	Gold	Silver
ω_p	Plasma frequency	1.3×10^{16} Hz [13]	1.4×10^{16} Hz [46]
γ_{bulk}	Damping constant	1.4×10^{14} Hz [44]	3.23×10^{13} Hz [46]
v_F	Fermi velocity	1.41×10^{15} nm $\cdot$ s^{-1} [13]	1.39×10^{15} nm $\cdot$ s^{-1} [47]
A	Scattering constant	0.25 [44]	1 [48]

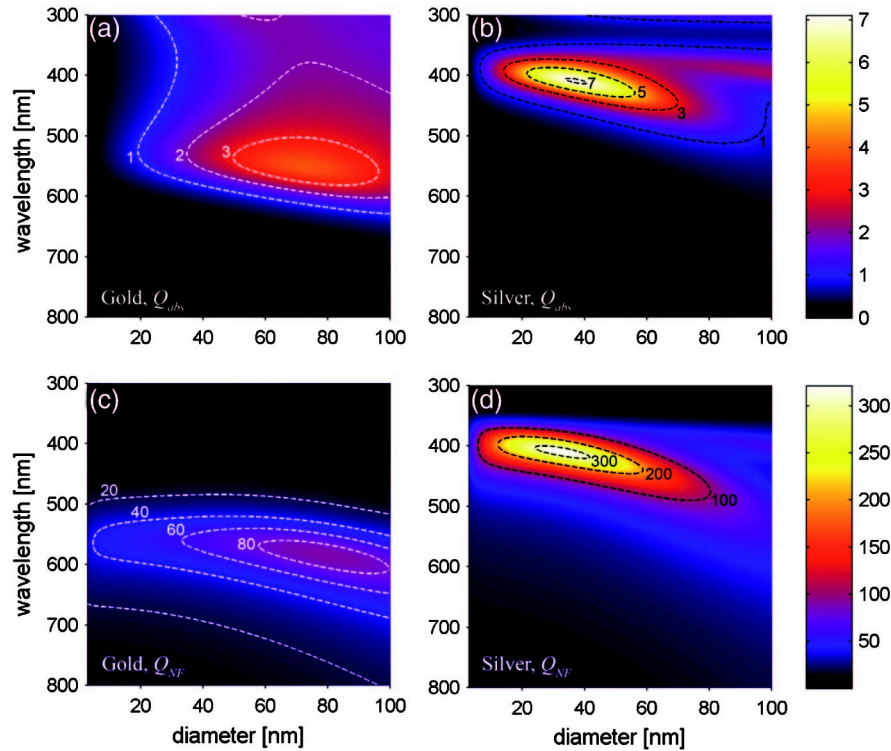Fig. 2.   Calculated Mie efficiencies of gold and silver nanospheres in water for various particle diameters and wavelengths, including the size-dependant correction for the dielectric constant. (a) Absorption efficiency of gold nanospheres. (b) Absorption efficiency of silver nanospheres. (c) Near-field efficiency of gold nanospheres. (d) Near-field efficiency of silver nanospheres.

$$x = 2\pi \frac{a}{\lambda_0} \sqrt{\varepsilon_m}, \tag{7}$$

and the scattering coefficients a_l and b_l are given by [42,49]

$$a_l = \frac{m\psi_l(mx)\psi'_l(x) - \psi_l(x)\psi'_l(mx)}{m\psi_l(mx)\xi'_l(x) - \xi_l(x)\psi'_l(mx)} \tag{8}$$

and

$$b_l = \frac{\psi_l(mx)\psi'_l(x) - m\psi_l(x)\psi'_l(mx)}{\psi_l(mx)\xi'_l(x) - m\xi_l(x)\psi'_l(mx)}, \tag{9}$$

where $m = (\varepsilon_p/\varepsilon_m)^{1/2}$, and ψ_l and ξ_l are the Riccati–Bessel functions of order l.

An additional important quantity for the light scattered by a noble-metal nanoparticle is the near-field efficiency, denoted by Q_{NF}, which represents the ability of the particle to convert the incident wave into light intensity near its surface [27,50]:

$$Q_{NF} = 2 \sum_{l=1}^{\infty} \left\{ |a_l|^2 \left[(l+1)|h_{l-1}^{(1)}(ka)|^2 + l|h_{l+1}^{(1)}(ka)|^2 \right] \right.$$
$$\left. + (2l+1)|b_l|^2|h_l^{(1)}(ka)|^2 \right\}, \tag{10}$$

where $h_l^{(1)}$ represents the spherical Henkel function of the first kind of order l.

The absorption efficiencies [Eq. (6)] for gold and silver nanoparticles in water ($\varepsilon_m = 1.78$) are plotted in Figs. 2(a) and 2(b), respectively, for different pulse central wavelengths and particle diameters. Similarly, the near-field efficiencies [Eq. (10)] for gold and silver nanoparticles are plotted in

Figs. 2(c) and 2(d), respectively. As was noted elsewhere [36], the absorption and near-field efficiencies exhibit different maxima for different wavelengths and diameters. For gold, the maximal absorption is obtained for 72 nm diameter particles at 550 nm wavelength, whereas the maximal near-field enhancement is obtained for 79 nm diameter particles at 585 nm wavelength. For silver, the maximum absorption and near-field enhancement are both obtained at a similar wavelength (409 nm) but for different particles diameters (37 nm and 32 nm, respectively). The effect of the small size of the nanoparticles [Eqs. (2) and (3)] becomes significant only for particles with diameters shorter than 7 nm [45], manifested by a noticeable decrease in both absorption and near-field enhancement (Fig. 2).

The wavelengths that yield the maximal absorption (λ_{abs}) and maximal near-field efficiencies (λ_{NF}) are plotted in Fig. 3(a) by solid and dashed curves, respectively, as a function of the gold (blue) and silver (red) particle diameters. Note the consistent red shift for both metals between the wavelengths of maximal near-field efficiency and of maximal absorption; the maximal absorption of a 50 nm in diameter gold nanoparticle is obtained at 536 nm wavelength, whereas the maximal near-field enhancement occurs at 565 nm. Thus, for the initiation of processes such as multiphoton ionization, which require high instantaneous intensities, choosing a pulse central wavelength that equals λ_{NF} would increase efficiency and reduce undesired thermal effects due to light absorption by the particle. While for silver nanoparticles of diameters smaller than 80 nm, the maximal absorption efficiency at λ_{abs} [Fig. 3(b), solid curves] is not much different compared to its value for λ_{NF} [Fig. 3(b), dashed curves], it drops in gold nanoparticles by nearly 30% at λ_{NF} for all particle diameters.
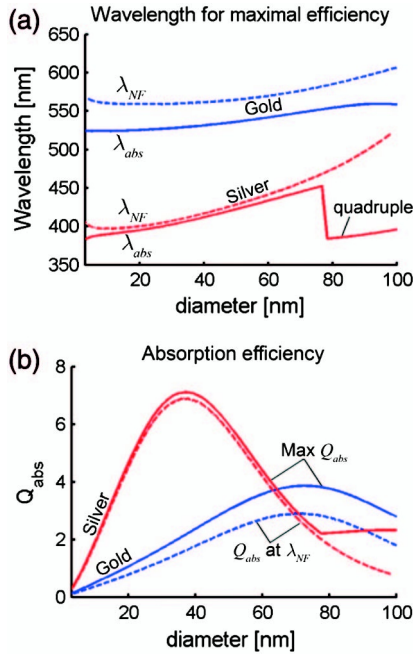
Fig. 3. (a) Wavelength of maximal absorption efficiency (solid curves) and maximal near-field efficiency (dashed), for gold (blue) and silver (red) nanospheres. (b) Maximum absorption efficiency (solid curves) and the absorption efficiency at λ_{NF} (dashed), for gold (blue) and silver (red) nanospheres.

For silver particles of diameters larger than 80 nm, the quadruple oscillation term becomes more significant than the dipole term, as seen in Figs. 2(b) and 2(d) for wavelengths between 380 nm and 400 nm. These quadruple oscillations result in a transition to shorter wavelength values for λ_{abs} [Fig. 3(a)] and a more pronounced difference between the absorption at λ_{NF} and λ_{abs} wavelengths [Fig. 3(b)].

The ratio between the scattered and the incident electric fields near particles with diameters of 5 nm, 20 nm, and 50 nm

are plotted for gold nanospheres in Figs. 4(a), 4(b), and 4(c), respectively, and for silver nanospheres in Figs. 4(d), 4(e), and 4(f), at illumination wavelengths that yield the maximum near-field enhancement [λ_{NF}; see Fig. 3(a)]. In all cases, the scattered intensity decays to its $1/e$ value at a distance that equals approximately one-tenth of the particle's diameter [illustrated by a dashed gray line in Fig. 4(f)]. The optical fields are nearly symmetric in both x and z axes for all cases, where the dipole approximation dominates the solution; the small quadruple contribution is noticeable as a slight shift of the field pattern toward positive z values (the propagation direction of the incident wave).

3. FREE ELECTRON DENSITY

The interaction of intense short laser pulses with biological media could lead to plasma formation through various physical processes, including multiphoton ionization, quantum tunneling, and impact (or cascade) ionization by excited electrons [32,40,51]. When the density of the excited electrons ("ionized free electrons") reaches above a critical value of approximately 10^{21} cm^{-3} [32], an optical breakdown occurs that involves the breakage of nearby molecular and atomic bonds. It has been shown experimentally that thresholds for optical breakdown in water are similar to those in other biological media [4,32]. For the purpose of obtaining a generic picture of the free electron density for different pulse durations, we assume that multiphoton and cascade ionization are the dominant mechanisms for the production of excited electrons [40,51], whereas losses of free electrons are primarily due to recombination and diffusion outside the interaction volume. Thus, the governing rate equation for the time evolution of the free electron density ρ is given by [51]

$$\frac{d\rho}{dt} = \eta_{MPI} + \eta_{casc}\rho_c - \eta_{diff}\rho - \eta_{rec}\rho^2. \qquad (11)$$
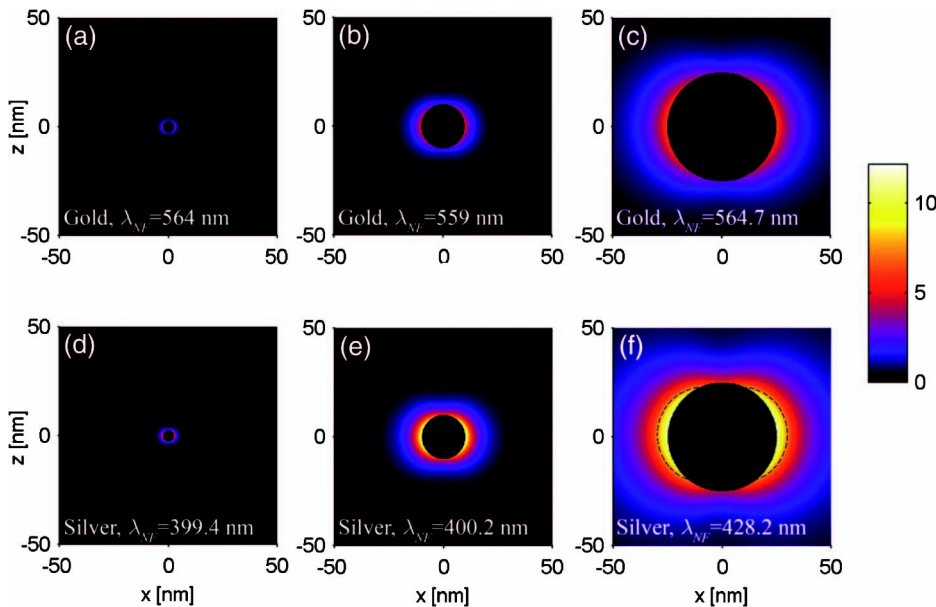

Fig. 4. Near-field enhancement factor (scattered field amplitude divided by incident field amplitude) at λ_{NF} (see text), including the size-dependant correction for the dielectric constant. (a) gold, 5 nm diameter, (b) gold, 20 nm diameter, (c) gold, 50 nm diameter (d) silver, 5 nm diameter, (e) silver, 20 nm diameter, (f) silver, 50 nm diameter. The region where the near-field enhancement factor is higher than its $1/e^{1/2}$ value is marked by a gray dashed line in (f).

The first two terms in Eq. (11) correspond to the contributions of multiphoton ionization and cascade ionization, where η_{MPI} and η_{casc} denote the rate coefficients of these processes, respectively. The third term in Eq. (11) corresponds to diffusion losses [51,52] with a diffusion rate η_{diff} given by

$$\eta_{\mathrm{diff}} = \frac{2E_{\mathrm{av}}\tau}{3m\Lambda^2}, \qquad (12)$$

where E_{av} denotes the average electron energy [32], $\tau = 1.7$ fs is the mean free time between collisions [53], m denotes the mass of an electron, and Λ denotes the characteristic diffusion length. In this work, we approximate the diffusion length as the radius of the nanospheres, which is the approximate length of the high intensity near-field region [see Fig. 4(f)]; free electrons that diffuse away from the interaction volume around the particle are removed from the total count of free electrons. The fourth term in Eq. (11) corresponds to losses due to electron-hole recombination, where an empirical rate value of $\eta_{\mathrm{rec}} = 2 \times 10^{-9}$ cm$^3 \cdot$ sec^{-1} is being used [54].

The multiphoton rate coefficient η_{MPI} is calculated according to [40]

$$\eta_{\mathrm{MPI}} = \frac{2\omega_0}{9\pi}\left(\frac{m'\omega_0}{\hbar}\right)^{\frac{3}{2}}\left[\frac{e^2}{16m'\Delta\omega_0^2 c\varepsilon_0 n_m}I(t)\right]^k$$
$$\times \exp(2k)\Phi\left(\sqrt{2k - \frac{2\Delta}{\hbar\omega_0}}\right), \qquad (13)$$

where

$$\Phi(x) = \int_0^x e^{y^2 - x^2}\,\mathrm{d}y. \qquad (14)$$

m' denotes the reduced mass, e the electron charge, c the speed of light, ε_0 the vacuum permittivity, n_m the refractive index of the medium, and $I(t)$ the light intensity; $\Delta = 6.5$ eV is the band gap for water [55], and $k = \lfloor \Delta/(\hbar\omega) + 1\rfloor$ is the number of photons needed to excite one electron across the band gap ($\lfloor x \rfloor$ denotes an integer part of x). The light intensity $I(t)$ in Eq. (13) is calculated according to $I(t) = NI_p(t)$, where $I_p(t)$ denotes the laser intensity and N denotes the average intensity enhancement over the interaction volume, near the nanoparticle.

After the first free electron is produced within the interaction volume, it gains sufficient energy for impact ionization by absorbing additional photons, resulting in cascade ionization with rate coefficient that equals [32]

$$\eta_{\mathrm{casc}} = \begin{cases} \frac{\eta}{1+\eta(t-\tau_{\mathrm{ion}})} & \rho_c V \geq \frac{1}{2} \\ 0 & \rho_c V < \frac{1}{2} \end{cases}, \qquad (15)$$

where $\tau_{\mathrm{ion}} = k\tau$ is the time during which the electrons accelerate, ρ_c denotes the electron density at time $t - \tau_{\mathrm{ion}}$, and V denotes the interaction volume for nanospheres. For the purpose of this derivation, V is the volume of the high field enhancement around the particle, whose cross section in the x-z plane is illustrated by a dashed gray line in Fig. 4(f). The coefficient η in Eq. (15) is given by [40]

$$\eta = \frac{1}{\omega_0^2\tau^2 + 1}\left(\frac{e^2\tau}{cn_m\varepsilon_0 m\Delta}I(t) - \frac{m\omega_0^2\tau}{M}\right), \qquad (16)$$

where M denotes the mass of a water molecule. The first term in Eq. (16) describes the energy gain due to photon absorption by the electrons during the laser pulse, and the second term represents energy loss through collisions with the heavy water molecules [40]. An average electron energy $E_{\mathrm{av}} = 5\Delta/4$ was used for calculating Eq. (12) [32].

Equation (11) was numerically solved (Matlab®) assuming a Gaussian temporal shape of duration τ_p:

$$I_p(t) = I_0 \exp\left[-4 \ln 2\left(\frac{t}{\tau_p}\right)^2\right], \qquad (17)$$

where I_0 denotes the peak irradiance of the pulse.

The temporal evolution of the free electron density near 50 nm diameter gold nanoparticles was calculated for different pulse durations and minimal peak irradiance $I_0 = I_{\mathrm{th}}$ values that are sufficient for generating the critical free electron density of 10^{21} cm^{-3} [32] (Fig. 5, solid blue curves). The horizontal time axes in Fig. 5 are normalized by the pulse duration in each case, and the corresponding threshold peak intensities of the pulses (I_{th}) are shown in each panel. In order to emphasize the role of cascade ionization, we also plot (dashed curves) the solutions to Eq. (11) without cascade ionization, by setting $\eta_{\mathrm{cas}} = 0$ in the second term of the right-hand side [40]. Note that cascade ionization is important for pulses in the picosecond range, where the total electron density is nearly 4 orders of magnitude higher than the density produced by multiphoton ionization alone. For pulses in the femtosecond range, on the other hand, cascade ionization is less significant and rapidly decreases for shorter pulses. Compared to the simulation results obtained by Vogel et al. [32] for tightly focused pulses in water, the threshold values for optical breakdown mediated by gold nanoparticles are lower by at least 1 order of magnitude owing to the contribution of the resonant near-field enhancement, despite the extremely small interaction volumes involved. At the irradiance thresholds, cascade ionization dominates the interaction for pulses longer than 10 fs in both cases, but is considerably less prevalent with the noble-metal nanoparticles.

The ratio between the total free electron density and the density produced by multiphoton ionization alone is plotted in Fig. 6 for gold (blue lines) and silver (red lines) nanospheres of 50 nm (solid line), 20 nm (dashed line), and 5 nm (dashed-dotted line) in diameter. Clearly, the contribution of cascade ionization is more significant for larger nanospheres, primarily due to the larger interaction volumes that require lower densities for initiating the avalanche process. The ratio between cascade and multiphoton ionization is also somewhat lower for silver particles (Fig. 6) due to their shorter resonant wavelengths, which result in a more efficient multiphoton ionization. By plotting (Fig. 7) the number of free electrons in the interaction volumes around 50 nm gold (blue lines) and silver (red lines) particles, we note that the sharp intensity thresholds characteristic of the 100 ps pulse (dashed lines) is less pronounced when using shorter 1 ps (dashed-dotted lines) and 50 fs (solid lines) pulses. This is because shorter pulses can produce significant densities of free electrons without cascade ionization, which requires pulses much
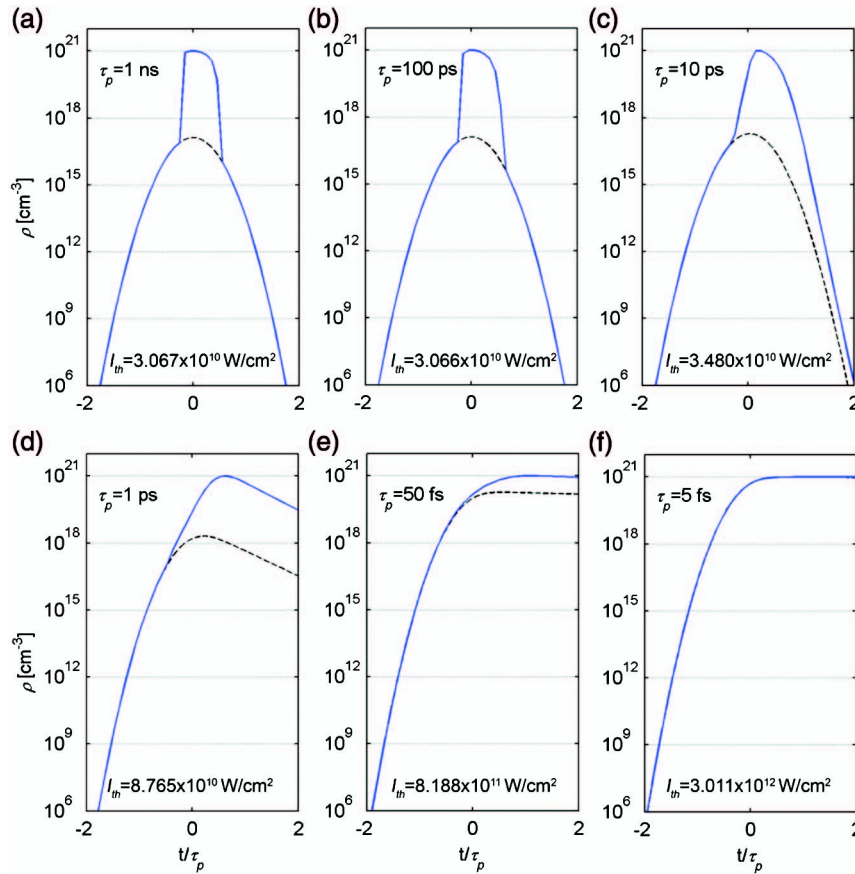
Fig. 5.   Free electron density near 50 nm diameter gold nanoparticles as a function of time normalized by pulse duration with (blue solid line) and without (dashed line) cascade ionization. (a) $\tau_p = 1$ ns. (b) $\tau_p = 100$ ps. (c) $\tau_p = 10$ ps. (d) $\tau_p = 1$ ps. (e) $\tau_p = 50$ fs. (f) $\tau_p = 5$ fs.
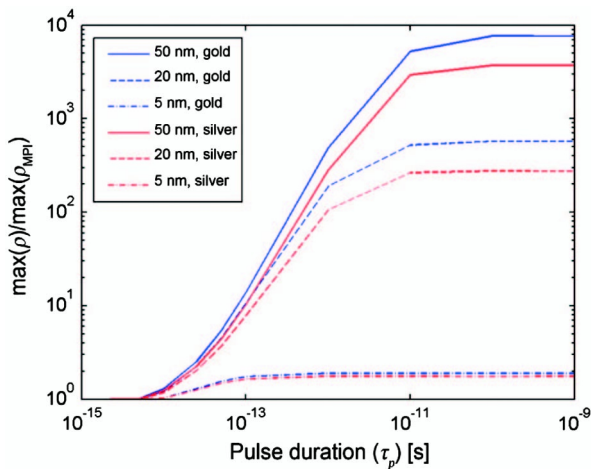

Fig. 6.   Ratio between the maximal free electron density with and without cascade ionization for gold (blue) and silver (red) nanoparticles with diameters of 50 nm (solid), 20 nm (dashed), and 5 nm (dotted dashed line).
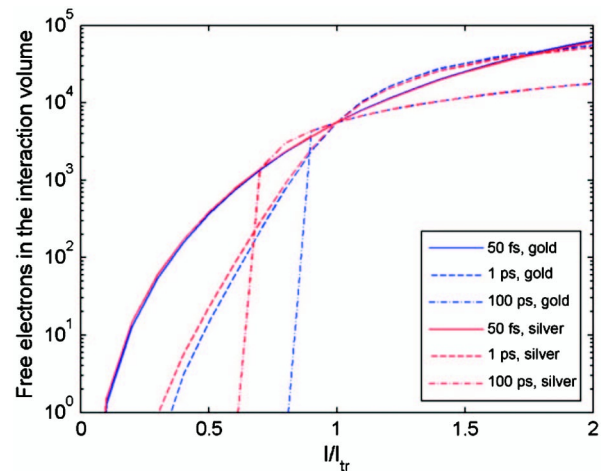

Fig. 7.   Total number of free electrons in the interaction volume as a function of pulse irradiance (normalized by its threshold intensity) for pulse durations of 50 fs (solid), 1 ps (dashed), and 100 ps (dashed-dotted line), for gold (blue) and silver (red) nanospheres. Sphere diameter is 50 nm. Wavelength is equal to λ_{NF} (maximum near-field efficiency).

longer than the time required for a single impact ionization event.

4. NANOPARTICLES TEMPERATURE

The light energy absorbed by a nanosphere E_{abs} is related to its absorption efficiency Q_{abs} according to

$$E_{abs} = I_{pulse}\pi a^2 Q_{abs}, \qquad (18)$$

where $I_{pulse} = I_0\tau_p[\pi/(4\ln 2)]^{1/2}$ is the total irradiance of the Gaussian pulse of Eq. (17). For calculating the temperature of the nanospheres after a single pulse illumination, the absorbed light energy is assumed to spread uniformly within
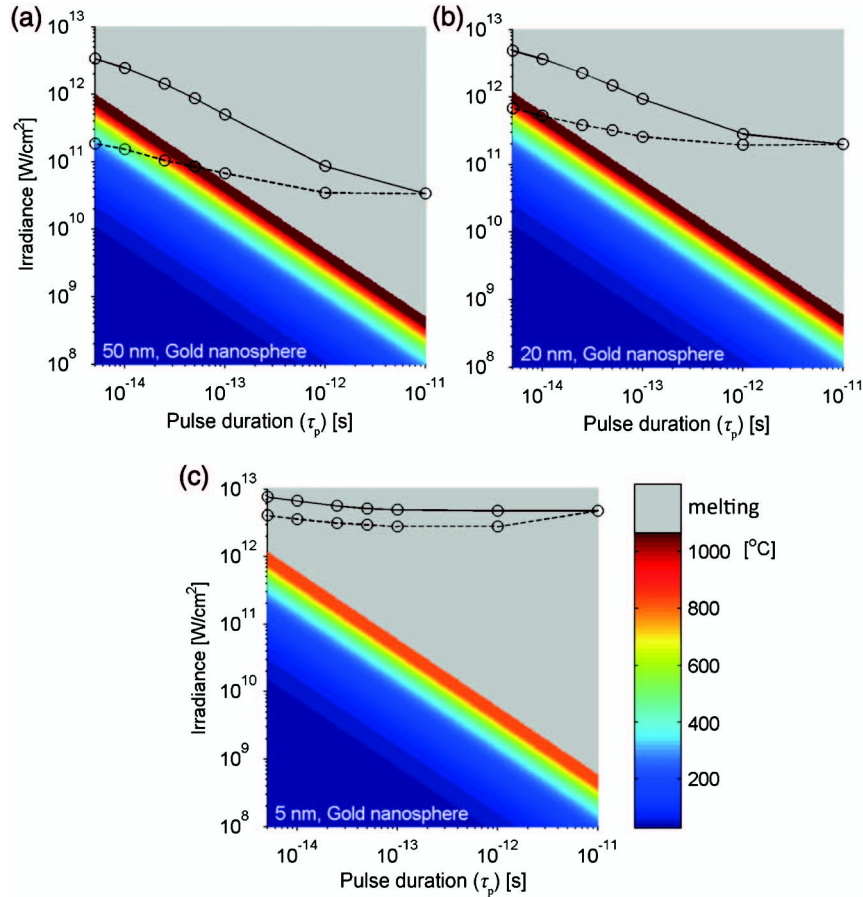
Fig. 8. Temperature of gold nanospheres as a function of pulse duration and irradiance. Solid lines connect between irradiance threshold values (circles) for optical breakdown, corresponding to free electron density of 10^{21} cm^{-3}. Dashed lines connect between irradiance threshold values for the generation of a single free electron within the interaction volume. (a) 50 nm diameter sphere. (b) 20 nm sphere. (c) 5 nm sphere.

the particle [35]. Heat dissipation to the surrounding medium can be neglected since the pulse durations considered for these calculations are equal to or much shorter than the typical time scale required for heat transfer from the nanoparticle to its surroundings (approximately 10 ps [25]). The melting temperature of nanospheres is generally size dependent and has been shown to be lower than the bulk melting temperature for small particle diameters [56,57]. For gold nanospheres above 20 nm in diameter, the melting temperature approaches the bulk value (1337 °K [58]), whereas for 5 nm diameter particles, the melting temperature reduces to approximately 1100 °K [56]. For silver particles, the melting temperature of nanospheres with diameters above 20 nm is also close (within less than 5%) to the bulk temperature of 1234 °K [58], whereas for 5 nm diameter particles the melting point is approximately 1000 °K [57]. Below the melting temperature, denoted here by T_m, the final temperature T of the nanoparticles is given by [35]

$$T = \begin{cases} \frac{E_{abs}}{c_p m_{np}} + T_0 & E_{abs} \leq E_m \\ T_m & E_m < E_{abs} < E_m + m_{np}\Delta H_{fus} \end{cases}, \quad (19)$$

where c_p denotes the heat capacity (0.129 J·g^{-1}·K^{-1} and 0.235 J·g^{-1}·K^{-1} for gold and silver, respectively [58]), m_{np} denotes the mass of the nanoparticle, T_0 denotes the particle

temperature before illumination, and $E_m = c_p m_{np}(T_m - T_0)$ is the energy needed to heat a particle from its initial temperature to T_m. For our calculations, the bulk values of the enthalpy of fusion at the melting point, denoted by ΔH_{fus}, were used for gold [56] and 20 nm or larger silver nanospheres [57] (64 J·g^{-1} and 104.76 J·g^{-1} for gold [25] and silver [58], respectively), whereas for 5 nm silver nanospheres, we have used a noticeably lower enthalpy value of 74.16 J·g^{-1} [57]. For absorbed energies above those referred to in Eq. (19), the particles may disintegrate [35,36] and/or undergo dramatic physical changes that cannot be described by a single temperature parameter.

The temperature of a gold nanoparticle was calculated for a single pulse illumination at resonant wavelength for maximum near-field enhancement, and is plotted as a function of pulse duration and irradiance in Figs. 8(a), 8(b), and 8(c) for 50 nm, 20 nm, and 5 nm diameter particles, respectively. Gold particles of 50 nm, 20 nm, and 5 nm in diameter reach their melting point at fluence values of 3.8×10^{-3} J/cm^2, 4.4×10^{-3} J/cm^2, and 4×10^{-3} J/cm^2, respectively, as manifested by the linear diagonal colored pattern in the plots. The regions corresponding to particle temperature above the melting point [Eq. (19)] are gray colored in the figures. Also plotted in Figs. 8(a)–8(c) are the irradiance thresholds for optical breakdown (I_{th} [see Figs. 5(a)–5(f)] (solid line) and for producing a single free electron within the interaction volume (dashed line). For 10 ps
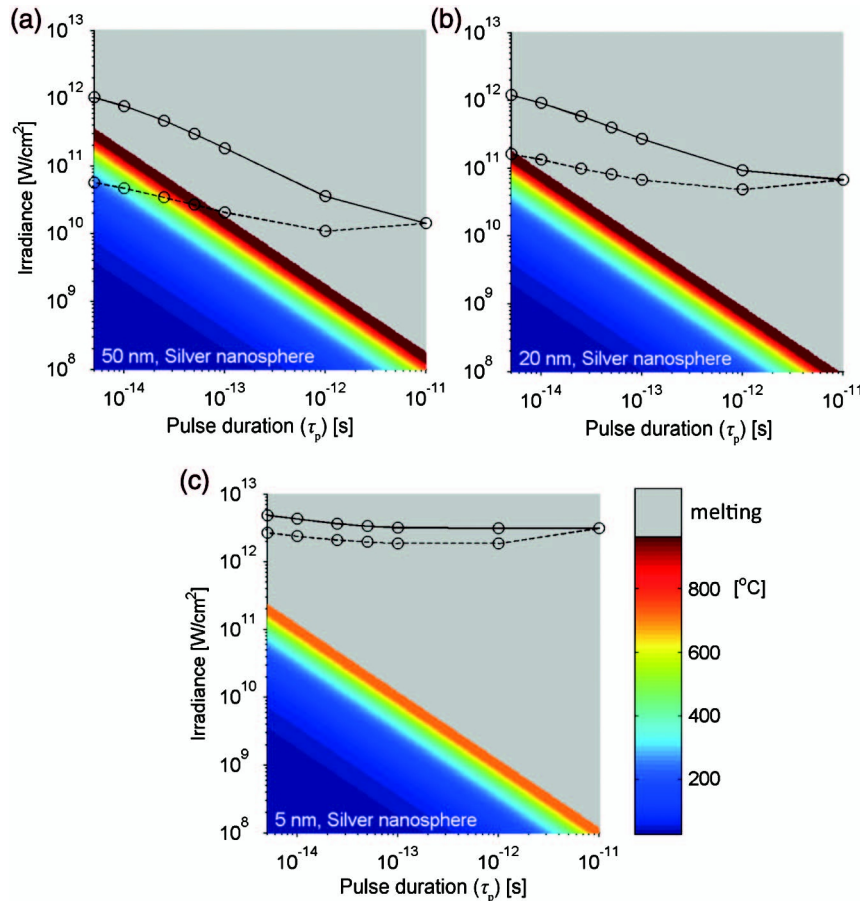
Fig. 9.   Temperature of silver nanospheres as a function of pulse duration and irradiance. Solid lines connect between irradiance threshold values (circles) for optical breakdown, corresponding to free electron density of 10^{21} cm^{-3}. Dashed lines connect between irradiance threshold values for the generation of a single free electron within the interaction volume. (a) 50 nm diameter sphere. (b) 20 nm sphere. (c) 5 nm sphere.

pulses and longer, both threshold values are virtually equal since the free electron density increases rapidly as soon as the first electron is produced (Fig. 7). Similarly, the temperature of silver particles, and the intensity thresholds for optical breakdown and first electron ionization, are plotted for particles of 50 nm, 20 nm, and 5 nm in diameter in Figs. 9(a), 9(b), and 9(c), respectively. Silver particles of 50 nm, 20 nm, and 5 nm in diameter reach their melting point at fluence values of 1.3×10^{-3} J/cm^2, 6.76×10^{-4} J/cm^2, and 9.14×10^{-4} J/cm^2, respectively. In comparison with gold nanoparticles (Fig. 8), silver nanoparticles require lower fluence values for reaching their melting point and for producing free electrons through multiphoton ionization.

It is evident from Figs. 8 and 9 that optical breakdown (solid lines) in the vicinity of gold and silver nanospheres is always accompanied by particle melting, even for pulses as short as 5 fs. When gold or silver nanospheres melt and later solidify (after the pulse), their overall shape is not significantly affected, and so are their optical properties. Therefore, nanospheres would inflict consistent damage to their vicinity (acoustic bubble and/or free electrons) even for a long series of pulses. Nonspherical particles such as nanorods, on the other hand, may lose their original shape [35] and consequently change their optical and mechanical properties.

In order to better understand the potential of gold nanorods to mediate a nanometric effect to their environment, we have used the field enhancement and absorption efficiencies calculated by Liu et al. [59], who applied a finite-difference time-domain method for simulating the interaction between a nanorod and resonant continuous-wave irradiation polarized along its major axis. These nanorods were chosen to have a resonance frequency at 808 nm, with a short axis length of 14 nm, an aspect ratio of 4.1, and an absorption efficiency of $Q_{abs} = 31$ [59]. Liu et al. [59] also calculated the volume in which the intensity enhancement exceeds 1000, which is approximately $1/(2e)$ of its maximum value at the particle surface; this volume is used here for estimating the interaction volume around the nanorod. Finally, the electron diffusion length was set equal to the short radius of the nanorod, $\Lambda = 7$ nm. The temperature of a gold nanorod after a single pulse illumination is plotted in Fig. 10 for different pulse intensities and durations, together with the threshold intensities for optical breakdown (solid line) and for a single multiphoton ionization event (dashed line). Evidently, the gold nanorod (14 nm diameter, 4.1 aspect ratio) has a much larger geometrical cross section than that of a gold nanosphere with the same volume; its high cross section to volume ratio, combined with its high absorption efficiency, results in particle melting at much lower fluence value of 8.88×10^{-5} J/cm^2. Here too, optical breakdown (solid line) near a nanorod would always be accompanied by particle melting, regardless of pulse duration.
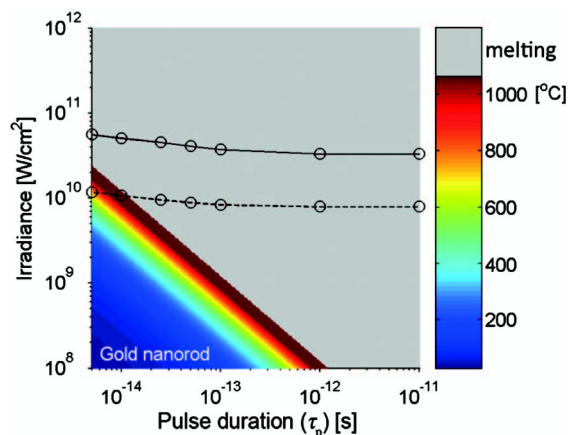
Fig. 10. Temperature of gold nanorod of 14 nm in diameter with aspect ratio of 4.1, as a function of pulse duration and irradiance. Solid lines connect between irradiance threshold values (circles) for optical breakdown, corresponding to free electron density of 10^{21} cm^{-3}. Dashed lines connect between irradiance threshold values for the generation of a single free electron within the interaction volume.

5. DISCUSSION

The term "nanomanipulation" of matter generally refers to the spatial extent of an induced physical process, and should not be confused with the dimensions of the particles that generate it. One approach for achieving small interaction volumes is to illuminate a light absorbing nanoparticle with pulses much shorter than the time needed for the heat to diffuse from the particle. Ultrashort pulses in the femtosecond range can also incorporate high-intensity-related processes, which may improve efficiency and locality of the interaction. Shown in Fig. 11 is a phase diagram that spans the various effects around a noble-metal nanoparticle illuminated by a single short pulse. Above certain irradiation thresholds (dotted line), the absorbed energy of the pulse is converted into a vapor bubble and an acoustic shock wave that extends over a few tens of nanometers from the particle [26]. Such vapor bubbles would often be accompanied by particle melting (dark red region) but could also occur below the melting point (transparent red hue) for particles of diameters larger than 30 nm [60]. Taking advantage of the strong field enhancement near the particle's surface, free electrons could be generated above certain intensities (dashed line), even without causing particle melting (green region). By itself, near-field enhancement is extremely local (see Fig. 4) and could affect volumes as small as 0.1 zepto-liters (zepto = 10^{-21}) through multiphoton ionization. At such short pulses, the transition to cascade ionization and optical breakdown (dashed-dotted line) would occur only for much more intense pulses, a process that would probably reduce the locality of the damage due to the high energies that are involved.
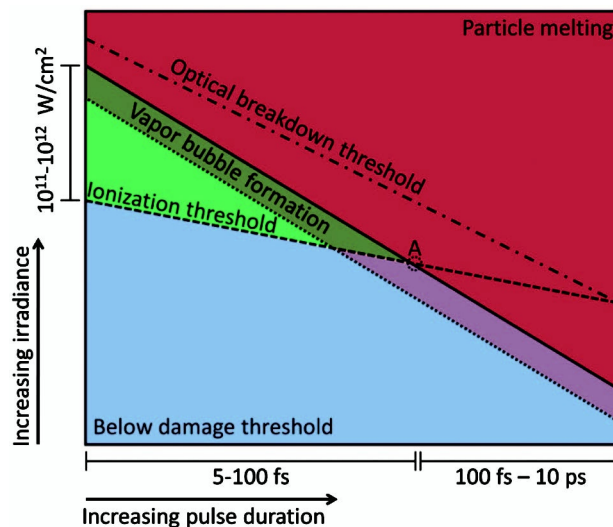

Fig. 11. Generalized phase diagram of the various processes induced by optical pulses of different durations and irradiance levels illuminating gold and silver nanoparticles.

We find that local multiphoton ionization with minimal heating and no optical breakdown could occur only within a very small experimental parameter space. In fact, such an effect is not possible for 5 nm gold and silver particles [Figs. 8(c) and 9(c)] and would involve significant heating of 20 nm diameter gold and silver particles [see Figs. 8(b) and 9(b)]. The tested nanorod [59] would also be incapable of inducing multiphoton ionization without significant heating or melting (Fig. 10). Nevertheless, particles 50 nm in diameter do allow such a process to take place; pulses shorter than 10 fs will heat both gold and silver particles to less than 400 °C, and could have sufficient irradiance for multiphoton ionization without initiating cascade ionization. Higher pulse irradiances would cause optical breakdown near 50 nm particles, always accompanied by particle melting as well. The point in the phase diagram that represents the transition from heat related processes to processes with free electrons generated by multiphoton ionization is marked by the dotted circle A in the figure. The transition points for gold and silver nanoparticles and for the gold nanorod are summarized in Table 2.

Note that the calculations in this work assumed aquatic environment to the particles, using the refractive index of water ($n = 1.33$). In a biological tissue, however, the refractive index may vary between $n = 1.34$ and $n = 1.55$ [61–63], which would have an effect on some key parameters of our results. For an average tissue refractive index of $n = 1.4$ [62], λ_{NF} would be only slightly longer than that obtained for water environment (by approximately 2% and 3.4% for gold and silver nanospheres, respectively), the absorption efficiency at

Table 2. Calculated Parameters of the Transition Point A in Fig. 11 (See Text)

		Gold	Silver
50 nm nanosphere	Water	$(70 \text{ fs}, 7.7 \times 10^{10} \text{ W/cm}^2)$	$(80 \text{ fs}, 2.3 \times 10^{10} \text{ W/cm}^2)$
	Tissue	$(70 \text{ fs}, 5.9 \times 10^{10} \text{ W/cm}^2)$	$(90 \text{ fs}, 2 \times 10^{10} \text{ W/cm}^2)$
20 nm nanosphere	Water	$(10 \text{ fs}, 4.7 \times 10^{11} \text{ W/cm}^2)$	$(5 \text{ fs}, 1.6 \times 10^{11} \text{ W/cm}^2)$
	Tissue	$(10 \text{ fs}, 4.2 \times 10^{11} \text{ W/cm}^2)$	$(5 \text{ fs}, 1.3 \times 10^{11} \text{ W/cm}^2)$
5 nm nanosphere		—	—
14 nm nanorod, 4.1 AR	Water	$(10 \text{ fs}, 1 \times 10^{10} \text{ W/cm}^2)$	

λ_{NF} would increase by a factor of approximately 1.26 and 1.06 for gold and silver nanospheres, respectively, and the local intensity enhancement would also increase by similar factors. As a result (see Table 2), lower fluence values would be required for melting the nanoparticles in tissue, and lower irradiance values (or longer pulses) would be sufficient to cause optical breakdown.

Most of the conclusions of this study rely on data drawn from numerous previous publications and several simplifying assumptions that were made. While most of the above calculations are linear, and thus provide fairly large error margins, the nonlinear nature of the multiphoton ionization process could be sensitive to small variations in the parameters that affect our light scattering calculations. We have found that an error in these parameters that would affect the calculated field-enhancement factors by 10% would result in approximately 20% change in the threshold irradiance values shown in Table 2, for both gold and silver particles. Other resulting parameters such as the resonance wavelengths and the threshold pulse durations (point A in Fig. 11) were only affected by approximately 10% or less.

The results obtained in this work could be useful in several research fields in chemistry and material science, and would be particularly attractive for various biomedical applications that call for specific interventions on a subcellular scale. For those applications, additional biologically related issues would need to be addressed. First, most biomedical applications require that the nanoparticles would be highly biocompatible, i.e., have low toxicity to cells and tissue. Gold nanoparticles are known to have low cytotoxicity [58,59], while silver nanoparticles are often considered toxic [64]. Both metals would usually benefit from a thin coating layer that would chemically isolate them from the environment and would be used to attach the particles to their targets. Such coating layers would be likely to be affected or damaged by any of the light-induced physical process described above. Second, the particle size would need to be carefully chosen to optimize the optical effect and, at the same time, allow for efficient particle delivery to its target. Fortunately, particles 50 nm in diameter, which were shown here as capable of inducing nanometric effects, could be effectively targeted to cancerous tumors through the enhanced permeability and retention (EPR) effect typical of blood vessels nourishing cancerous tissues [65]. Third, the illumination wavelength would have critical influence on the desired outcome; the blue resonant wavelength for small silver particles could be harmful to tissues and affect native tissue regions free of nanoparticles, while near infrared wavelength (resonance wavelength for nanorods) is generally considered nontoxic to living cells and could penetrate deep into a thick tissue. Finally, a single nanometric effect by a single pulse would most likely be too weak to affect its macroscopic environment; the quantity, concentration, and targeting accuracy of the nanoparticles would thus play critical roles in determining the total effect on a large heterogeneous tissue.

6. SUMMARY

In summary, by simulating the interactions between short pulses and noble-metal nanoparticles, we have explored a range of experimental parameters that affect the near environment of the particles. We show that while pulses in the nanosecond-picosecond range mainly heat the particle and its environment, femtosecond pulses can induce complex interactions that involve the generation of vapor bubbles, acoustic shock waves, multiphoton ionization, and optical breakdown. The delicate balance between these processes would eventually dictate the nature and the extent of the effect of the nanoparticle on its environment, while the total effect in the macroscopic scale would be highly sensitive to various experimental conditions such as illumination parameters and particle concentration.

ACKNOWLEDGMENTS

REFERENCES

1. R. R. Anderson and J. A. Parrish, "Selective photothermolysis: precise microsurgery by selective absorption of pulsed radiation," Science **220**, 524–527 (1983).
2. G. L. LeCarpentier, M. Motamedi, L. P. McMath, S. Rastegar, and A. J. Welch, "Continuous wave laser ablation of tissue: analysis of thermal and mechanical events," IEEE Trans. Biomed. Eng. **40**, 188–200 (1993).
3. M. A. Latina and C. Park, "Selective targeting of trabecular meshwork cells: in vitro studies of pulsed and CW laser interactions," Exp. Eye Res. **60**, 359–371 (1995).
4. V. Venugopalan, A. Guerra III, K. Nahen, and A. Vogel, "Role of laser-induced plasma formation in pulsed cellular microsurgery and micromanipulation," Phys. Rev. Lett. **88**, 078103 (2002).
5. V. Kohli, A. Y. Elezzabi, and J. P. Acker, "Cell nanosurgery using ultrashort (femtosecond) laser pulses: applications to membrane surgery and cell isolation," Lasers Surg. Med. **37**, 227–230 (2005).
6. K. König, I. Riemann, P. Fischer, and J. K. Halbhuber, "Intracellular nanosurgery with near infrared femtosecond laser pulses," Cell. Mol. Biol. **45**, 195–201 (1999).
7. N. Shen, D. Datta, C. B. Schaffer, P. LeDuc, D. E. Ingber, and E. Mazur, "Ablation of cytoskeletal filaments and mitochondria in live cells using a femtosecond laser nanoscissor," Mech. Chem. Biosyst. **2**, 17–25 (2005).
8. K. König, I. Riemann, and W. Fritzsche, "Nanodissection of human chromosomes with near-infrared femtosecond laser pulses," Opt. Lett. **26**, 819–821 (2001).
9. U. K. Tirlapur and K. Konig, "Cell biology: targeted transfection by femtosecond laser," Nature **418**, 290–291 (2002).
10. M. F. Yanik, H. Cinar, H. N. Cinar, A. D. Chisholm, Y. Jin, and A. Ben-Yakar, "Neurosurgery: functional regeneration after laser axotomy," Nature **432**, 822–822 (2004).
11. M. Hofmann, C. Eggeling, S. Jakobs, and S. W. Hell, "Breaking the diffraction barrier in fluorescence microscopy at low light intensities by using reversibly photoswitchable proteins," Proc. Natl. Acad. Sci. USA **102**, 17565–17569 (2005).
12. M. J. Rust, M. Bates, and X. Zhuang, "Sub-diffraction-limit imaging by stochastic optical reconstruction microscopy (STORM)," Nat. Methods **3**, 793–796 (2006).
13. C. G. Granqvist and O. Hunderi, "Optical properties of ultrafine gold particles," Phys. Rev. B **16**, 3513 (1977).
14. M. C. Daniel and D. Astruc, "Gold nanoparticles: assembly, supramolecular chemistry, quantum-size-related properties, and applications toward biology, catalysis, and nanotechnology," Chem. Rev. **104**, 293–346 (2004).
15. Yu-Ying Yu, S.-S. Chang, C.-L. Lee, and C. R. C. Wang, "Gold nanorods: electrochemical synthesis and optical properties," J. Phys. Chem. B **101**, 6661–6664 (1997).
16. P. K. Jain, I. H. El-Sayed, and M. A. El-Sayed, "Au nanoparticles target cancer," Nano Today **2**, 18–29 (2007).
17. D. Yelin, D. Oron, S. Thiberge, E. Moses, and Y. Silberberg, "Multiphoton plasmon-resonance microscopy," Opt. Express **11**, 1385–1391 (2003).

18. H. Wang, T. B. Huff, D. A. Zweifel, W. He, P. S. Low, A. Wei, and J.-X. Cheng, "In vitro and in vivo two-photon luminescence imaging of single gold nanorods," Proc. Natl. Acad. Sci. USA **102**, 15752–15756 (2005).

19. X. Huang, I. H. El-Sayed, W. Qian, and M. A. El-Sayed, "Cancer cell imaging and photothermal therapy in the near-infrared region by using gold nanorods," J. Am. Chem. Soc. **128**, 2115–2120 (2006).

20. T. S. Troutman, J. K. Barton, and M. Romanowski, "Optical coherence tomography with plasmon resonant nanorods of gold," Opt. Lett. **32**, 1438–1440 (2007).

21. D. Pissuwan, T. Niidome, and M. B. Cortie, "The forthcoming applications of gold nanoparticles in drug and gene delivery systems," J. Controlled Release **149**, 65–71 (2011).

22. G. F. Paciotti, L. Myer, D. Weinreich, D. Goia, N. Pavel, R. E. McLaughlin, and L. Tamarkin, "Colloidal gold: a novel nanoparticle vector for tumor directed drug delivery," Drug Deliv. **11**, 169–183 (2004).

23. C. Loo, A. Lowery, N. Halas, J. West, and R. Drezek, "Immuno-targeted nanoshells for integrated cancer imaging and therapy," Nano Lett. **5**, 709–711 (2005).

24. D. P. O'Neal, L. R. Hirsch, N. J. Halas, J. D. Payne, and J. L. West, "Photo-thermal tumor ablation in mice using near infrared-absorbing nanoparticles," Cancer Lett. **209**, 171–176 (2004).

25. O. Ekici, R. K. Harrison, N. J. Durr, D. S. Eversole, M. Lee, and A. Ben-Yakar, "Thermal analysis of gold nanorods heated with femtosecond laser pulses," J. Phys. D **41**, 185501 (2008).

26. A. N. Volkov, C. Sevilla, and L. V. Zhigilei, "Numerical modeling of short pulse laser interaction with Au nanoparticle surrounded by water," Appl. Surf. Sci. **253**, 6394–6399 (2007).

27. B. J. Messinger, K. U. von Raben, R. K. Chang, and P. W. Barber, "Local fields at the surface of noble-metal microspheres," Phys. Rev. B **24**, 649 (1981).

28. D. Eversole, B. Luk'yanchuk, and A. Ben-Yakar, "Plasmonic laser nanoablation of silicon by the scattering of femtosecond pulses near gold nanospheres," Appl. Phys. A **89**, 283–291 (2007).

29. W. Osamu, I. Taiji, H. Makoto, T. Masaaki, and K. Yoshimasa, "Nanofabrication induced by near-field exposure from a nanosecond laser pulse," Appl. Phys. Lett. **79**, 1366 (2001).

30. D. O. Lapotko, E. Lukianova, and A. A. Oraevsky, "Selective laser nano-thermolysis of human leukemia cells with microbubbles generated around clusters of gold nanoparticles," Lasers Surg. Med. **38**, 631–642 (2006).

31. Y. Cuiping, Q. Xiaochao, Z. Zhenxi, H. T. Gereon, and R. Ramtin, "Influence of laser parameters on nanoparticle-induced membrane permeabilization," **14**, 054034 J. Biomed. Opt. (2009).

32. A. Vogel, J. Noack, G. Hüttman, and G. Paltauf, "Mechanisms of femtosecond laser nanosurgery of cells and tissues," Appl. Phys. B **81**, 1015–1047 (2005).

33. N. N. Nedyalkov, H. Takada, and M. Obara, "Nanostructuring of silicon surface by femtosecond laser pulse mediated with enhanced near-field of gold nanoparticles," Appl. Phys. A **85**, 163–168 (2006).

34. A. Csaki, F. Garwe, A. Steinbruck, G. Maubach, G. Festag, A. Weise, I. Riemann, K. Konig, and W. Fritzsche, "A parallel approach for subwavelength molecular surgery using gene-specific positioned metal nanoparticles as laser light antennas," Nano Lett. **7**, 247–253 (2007).

35. S. Link, C. Burda, B. Nikoobakht, and M. A. El-Sayed, "Laser-induced shape changes of colloidal gold nanorods using femtosecond and nanosecond laser pulses," J. Phys. Chem. B **104**, 6152–6163 (2000).

36. O. Warshavski, L. Minai, G. Bisker, and D. Yelin, "Effect of single femtosecond pulses on gold nanoparticles," J. Phys. Chem. C **115**, 3910–3917 (2011).

37. H. Muto, K. Miyajima, and F. Mafune, "Mechanism of laser-induced size reduction of gold nanoparticles as studied by single and double laser pulse excitation," J. Phys. Chem. C **112**, 5810–5815 (2008).

38. A. Takami, H. Kurita, and S. Koda, "Laser-induced size reduction of noble metal particles," J. Phys. Chem. B **103**, 1226–1232 (1999).

39. E. Y. Lukianova-Hleb, A. P. Samaniego, J. Wen, L. S. Metelitsa, C.-C. Chang, and D. O. Lapotko, "Selective gene transfection of

40. individual cells in vitro with plasmonic nanobubbles," J. Control. Release **152**, 286–293 (2011).

40. J. Noack and A. Vogel, "Laser-induced plasma formation in water at nanosecond to femtosecond time scales: calculation of thresholds, absorption coefficients, and energy density," IEEE J. Quantum Electron. **35**, 1156–1167 (1999).

41. G. Mie, "Beiträge zur Optik trüber Medien, speziell kolloidaler Metallösungen," Ann. Phys. **330**, 377–445 (1908).

42. C. F. Bohren and D. R. Huffman, *Absorption and Scattering of Light by Small Particles* (Wiley-Interscience, 1983).

43. U. Kreibig and C. V. Fragstein, "The limitation of electron mean free path in small silver particles," Zeitschrift für Physik A **224**, 307–323 (1969).

44. S. P. Berciaud, L. Cognet, P. Tamarat, and B. Lounis, "Observation of intrinsic size effects in the optical response of individual gold nanoparticles," Nano Lett. **5**, 515–518 (2005).

45. B. S. Lucía and O. T. Jorge, "Size dependence of refractive index of gold nanoparticles," Nanotechnology **17**, 1309 (2006).

46. P. B. Johnson and R. W. Christy, "Optical constants of the noble metals," Phys. Rev. B **6**, 4370 (1972).

47. C. Kittel, *Introduction to Solid State Physics*, 7th ed. (Wiley, 1960).

48. T. Okamoto and S. Kawata, *Near-Field Optics and Surface Plasmon Polaritons* (Springer, 2001), pp. 97–123.

49. H. C. Hulst, *Light Scattering by Small Particles* (Courier Dover, 1981).

50. M. Quinten, "Local fields and Poynting vectors in the vicinity of the surface of small spherical particles," Zeitschrift für Physik D **35**, 217–224 (1995).

51. P. K. Kennedy, "A first-order model for computation of laser-induced breakdown thresholds in ocular and aqueous media. I. Theory," IEEE J. Quantum Electron. **31**, 2241–2249 (1995).

52. N. Kroll and K. M. Watson, "Theoretical study of ionization of air by intense laser pulses," Phys. Rev. A **5**, 1883 (1972).

53. Q. Sun, H. Jiang, Y. Liu, Z. Wu, H. Yang, and Q. Gong, "Measurement of the collision time of dense electronic plasma induced by a femtosecond laser in fused silica," Opt. Lett. **30**, 320–322 (2005).

54. F. Docchio, "Lifetimes of plasmas induced in liquids and ocular media by single Nd:YAG laser pulses of different duration," Europhys. Lett. **6**, 407 (1988).

55. W. Ferd, S. P. Varma, and S. Hillenius, "Liquid Water as a Lone-Pair Amorphous Semiconductor," J. Chem. Phys. **64**, 1549–1554 (1976).

56. P. Buffat and J. P. Borel, "Size effect on the melting temperature of gold particles," Phys. Rev. A **13**, 2287–2298 (1976).

57. W. Luo, W. Hu, and S. Xiao, "Size effect on the thermodynamic properties of silver nanoparticles," J. Phys. Chem. C **112**, 2359–2369 (2008).

58. W. M. Haynes, *CRC Handbook of Chemistry and Physics*, 91st ed. (CRC Press/Taylor and Francis, 2011).

59. M. Liu, P. Guyot-Sionnest, T.-W. Lee, and S. K. Gray, "Optical properties of rodlike and bipyramidal gold nanoparticles from three-dimensional computations," Phys. Rev. B **76**, 235428 (2007).

60. V. Kotaidis, C. Dahmen, G. von Plessen, F. Springer, and A. Plech, "Excitation of nanoscale vapor bubbles at the surface of gold nanoparticles in water," J. Chem. Phys. **124**, 184702–184707 (2006).

61. G. J. Tearney, M. E. Brezinski, J. F. Southern, B. E. Bouma, M. R. Hee, and J. G. Fujimoto, "Determination of the refractive index of highly scattering human tissue by optical coherence tomography," Opt. Lett. **20**, 2258–2260 (1995).

62. F. P. Bolin, L. E. Preuss, R. C. Taylor, and R. J. Ference, "Refractive index of some mammalian tissues using a fiber optic cladding method," Appl. Opt. **28**, 2297–2303 (1989).

63. J. M. Schmitt and A. Knüttel, "Model of optical coherence tomography of heterogeneous tissue," J. Opt. Soc. Am. A **14**, 1231–1242 (1997).

64. P. V. AshaRani, G. Low Kah Mun, M. P. Hande, and S. Valiyaveettil, "Cytotoxicity and genotoxicity of silver nanoparticles in human cells," ACS Nano **3**, 279–290 (2009).

65. A. K. Iyer, G. Khaled, J. Fang, and H. Maeda, "Exploiting the enhanced permeability and retention effect for tumor targeting," Drug Discov. Today **11**, 812–818 (2006).